Research Article Vol. 36, No. 6 / June 2019 / Journal of the Optical Society of America B 1645

Journal of the Optical Society of America B

OPTICAL PHYSICS

Polarization-selective defect mode amplification in a photonic crystal with intracavity 2D arrays of metallic nanoparticles

Sergey G. Moiseev,[1,2,3,*] Igor A. Glukhov,[1,4] Yuliya S. Dadoenkova,[1,4] and Florian F. L. Bentivegna[4]

[1]Ulyanovsk State University, Ulyanovsk 432017, Russia
[2]Ulyanovsk State Technical University, Ulyanovsk 432027, Russia
[3]Kotelnikov Institute of Radio Engineering and Electronics of the Russian Academy of Sciences, Ulyanovsk Branch, Ulyanovsk 432011, Russia
[4]Lab-STICC (UMR 6285), CNRS, ENIB, 29238 Brest Cedex 3, France
*Corresponding author: serg-moiseev@yandex.ru

Received 14 March 2019; revised 5 May 2019; accepted 7 May 2019; posted 9 May 2019 (Doc. ID 362328); published 29 May 2019

We demonstrate the possibility of polarization-selective amplification of a defect mode in an active multilayered photonic crystal through the resonant excitation of surface plasmons in a 2D ordered array of metallic nanoparticles embedded in the structure. Such an array acts as a polarizer whose spectral characteristics are defined by the shape of the nanoparticles and the periodicity of the array. The modal selectivity of the photonic structure is due to the strong surface-plasmon-assisted scattering of light by anisotropic nanoparticles, which depends on the relative orientations of their anisotropy axis and the polarization direction of the incoming light wave. The spectral and polarimetric characteristics of the photonic structure are calculated using the transfer matrix formalism. The 2D array of nanoparticles is described within the coupled-dipole approximation and is associated with a matrix whose elements depend on the geometry of the array and the polarization of the radiation. We show that in order to achieve defect mode amplification for a chosen polarization in such a heterostructure, the position of the array of nanoparticles should be made to coincide with regions of high optical field localization. We also determine the structural characteristics of the nanoparticle array that enhance the sensitivity of the spectral behavior of the photonic heterostructure to the polarization state of the incoming light beam.

https://doi.org/10.1364/JOSAB.36.001645

1. INTRODUCTION

A metallic nanoparticle (NP) interacting with an electromagnetic wave can support a localized surface plasmon resonance that gives rise to a characteristic peak in its extinction spectrum [1]. When metallic NPs are arranged in 2D or 3D arrays, they can efficiently modify the amplitude and the phase of an electromagnetic wave whose frequency is close to the plasmon resonance of the NPs [2–5]. It has been shown that the optical properties of such NP arrays depend on such factors as the nature of the metal; the size, shape, and surface/volume ratio of the NPs; as well as the periodicity of the array. The versatile plasmonic properties of metallic NP arrays have found many applications in the design of, among others, photonic crystals (PCs) [6–11], biological or medical sensors [12,13], antireflective coatings [14,15], and absorbers [16,17].

The polarimetric characteristics of light interaction with NP arrays have also been the topic of recent investigations [18–20]. For instance, the use of composite media with non-spherical metal inclusions has been shown to allow a polarization-sensitive control of the resonance modes of PC-based structures [21,22].

Such results can be useful in order to achieve a good control of the state of polarization of the radiation generated by vertical-cavity surface-emitting lasers (VCSELs), as such control remains a topical research subject. Indeed, because of the inherent symmetry of the resonant cavities of VCSELs, the light waves they emit do not have a well-defined state of polarization [23]. This results in the emission of radiation with uncontrolled polarization states and also in intensity instabilities. Various solutions have been put forward in order to eliminate such polarization-unstable behavior, notably inserting PCs, dielectric gratings, and plasmonic elements such as metallic films with nanoholes and metallic nanorod arrays in the aperture area of the VCSEL [24–29].

As is well known, PCs have been the subject of intensive theoretical and experimental investigations in the past decades because the control of electromagnetic waves that they provide can find many applications in modern photonics and optoelectronics [30,31]. Artificial PCs are one-, two-, or three-dimensional (1D, 2D, or 3D) structures that exhibit a periodic modulation of their permittivity and/or permeability (e.g., through the alternate juxtaposition of materials with different refractive indices).

The interaction between counterpropagating waves in such structures ensures the existence of their most prominent feature, photonic bandgaps in their transmittivity spectra, i.e., spectral domains for which the transmittivity is vanishingly small and the incident radiation is almost totally reflected. It is also well known that introducing elements into the PC that destroy their periodicity leads to the appearance of narrow peaks of high transmittivity (so-called defect modes) at frequencies located inside the photonic bandgap.

In [32], we demonstrated the possibility of polarization-selective generation in a 1D PC via the use of an embedded composite film consisting of an amplifying medium with chaotically distributed prolate metallic NPs. In this case, polarization selectivity is achieved due to the different absorption of the electromagnetic wave depending on the relative orientation of the anisotropy axes of NPs and the polarization direction of the wave.

In our aforementioned previous work [32], polarization selectivity was achieved using bulk (3D) random nanocomposite layers. In this paper, we intend to show that control of the polarization of an amplified defect mode transmitted through an active multilayered PC can be obtained by introducing one or several ordered 2D arrays of metallic (silver) NPs at well-chosen locations in the structure. The spectral and polarimetric characteristics of the heterostructure are calculated using the transfer matrix formalism, in which an embedded 2D NP array is associated with a matrix whose polarization-dependent elements are obtained within the frame of the coupled-dipole approximation approach. The influence of the geometry and location of the NP array(s) on the efficiency of polarization-selective defect mode amplification are discussed.

The paper is organized as follows. In Section 2, we describe the geometry of the photonic structure and define its material parameters. In Section 3, we present the derivation of its reflectivity and transmittivity based on the transfer matrix formalism. The numerical simulations of the spectral characteristics of a sole NP array, as well as those of the photonic crystal with and without a NP array, are shown and discussed in Section 4, and we summarize our conclusions in Section 5.

2. GEOMETRY OF THE STRUCTURE

Let us first consider the photonic structure without NP arrays. It is composed of two distributed Bragg reflectors (DBRs) surrounding a composite microcavity (Fig. 1). The DBRs are made of N unit cells (AB) and (BA), where A and B are layers of non-magnetic dielectric materials. The microcavity, denoted (CDC), consists of an active (amplifying) region D sandwiched between two identical non-magnetic dielectric layers C. The active region ensures the amplification of electromagnetic waves propagating through the structure, which is surrounded by a vacuum.

In the following, an incident plane wave in the near-infrared regime impinges under normal incidence on the left-hand side of the structure at abscissa $z = 0$ of a Cartesian coordinate system whose z axis is perpendicular to the interfaces of the system. The time dependence of the electromagnetic fields is taken as $\exp(-i\omega t)$, where $\omega = 2\pi c/\lambda_0$ is the angular frequency of the incoming plane wave of wavelength in a vacuum λ_0. The dimensions of the layers along the x and y axes are much larger

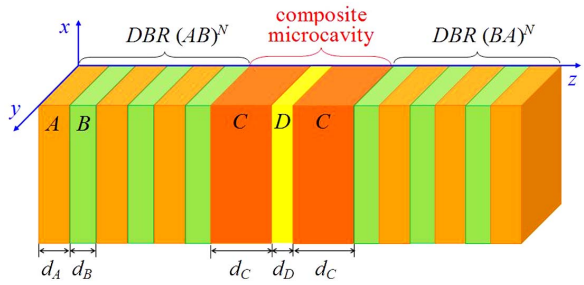

Fig. 1. Schematic of the structure: two DBRs $(AB)^N$ and $(BA)^N$ are separated by a composite microcavity consisting of an amplifying layer D surrounded by two identical cladding layers C.

than their thicknesses along the z axis and are thus taken to be infinite in the calculations.

Layers A and B (with thicknesses d_A and d_B, respectively) are made of isotropic, non-magnetic semiconductor materials GaAs and AlAs with dielectric permittivities ε_A and ε_B, respectively. Their thicknesses d_A and d_B satisfy the Bragg condition of resonant reflection at vacuum wavelength $\lambda_0 = 1.55$ μm as follows:

$$d_A\sqrt{\mathrm{Re}[\varepsilon_A]} = d_B\sqrt{\mathrm{Re}[\varepsilon_B]} = \frac{1.55}{4}\ \mu\mathrm{m}. \tag{1}$$

Each DBR consists of $N = 20$ GaAs/AlAs bilayers. As is well known, in the absence of the (CDC) microcavity, the transmission spectrum of the PC formed by the juxtaposition of those DBRs exhibits a photonic bandgap with a peak of transmittivity, or defect mode, centered on wavelength $\lambda_0 = 1.55$ μm because the central layer of a $(AB)^N(BA)^N$ PC (a defect layer with thickness $2d_B$) breaks the periodicity of the structure. Similarly, the presence of a defect layer consisting of the (CDC) microcavity typically introduces one or several defect modes inside the photonic bandgap. Here the cavity consists of two identical GaAs cladding layers (such that $\varepsilon_C = \varepsilon_A$ but with thickness $d_C \neq d_A$ in the most general case) surrounding an active region with an overall thickness d_D. The active region is a GaAs-based multiple quantum well VCSEL in which four $Ga_{0.591}In_{0.409}N_{0.028}As_{0.89}Sb_{0.08}$ quantum wells are separated by $GaN_{0.047}As$ barrier layers, similar to that described in Ref. [33]. Specifically, the constitution of the microcavity and its thickness $(d_D + 2d_C)$ are chosen such that it introduces a single defect mode centered on wavelength $\lambda_0 = 1.55$ μm.

The values of the material parameters and layer thicknesses used for our calculations are gathered in Table 1.

If, as is the case here, the thicknesses of the layers composing the active region are much smaller than the radiation wavelength, region D can be described with good accuracy by an average dielectric permittivity $\varepsilon_D = \varepsilon'_D + i\varepsilon''_D$ obtained within an effective medium approximation [35]. The amplification of an electromagnetic wave in this active equivalent layer, despite the optical absorption taking place in some of the layers of the structure, is described by $\varepsilon''_D < 0$.

Figure 2 shows the spatial distribution of the optical electric field amplitude along the z axis, obtained with transfer matrix calculations (see Section 3) and normalized with respect to the field amplitude of the incoming wave. This field exhibits three

Table 1. Material Permittivities and Layer Thicknesses Used for the Numerical Calculations

Medium		Permittivity at $\lambda_0 = 1.55$ μm		Layer Thickness (nm)	
A		$\varepsilon_A \approx 11.255 + i\ 0.027$ [34]		$d_A = 115.5$	
B		$\varepsilon_B \approx 8.36$ [29]		$d_B = 134$	
C		$\varepsilon_C \approx 11.255 + i0.027$ [34]		$d_C = 404$	
D	Quantum well	$\varepsilon_D \approx 12.869 - i0.214$	13.610 [33]	$d_D = 104$	8 [33]
	Barrier		12.557 [33]		24 [33]

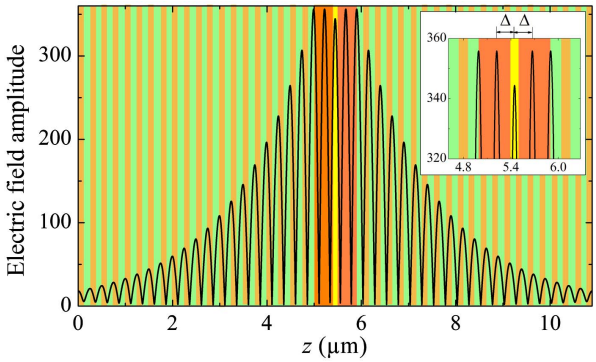

Fig. 2. Longitudinal distribution of the optical field amplitude (normalized with respect to the field amplitude of the incoming wave) in the photonic structure shown in Fig. 1. The colors of the vertical bars correspond to those of the layers in the schematic of the structure. The inset zooms in on the area immediately surrounding the composite microcavity. The distance Δ refers to the positions of two absolute field maxima inside the microresonator where the NP arrays can be embedded [as in Fig. 3(b)].

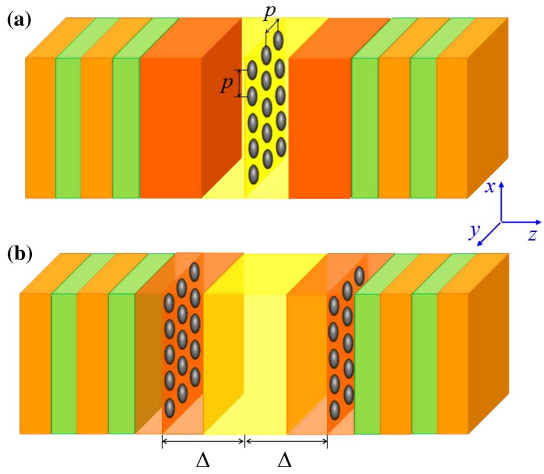

Fig. 3. Schematic of the photonic structure including 2D metallic NP arrays placed (a) at the center of the active region and (b) on both sides of the active region at distance $\Delta = \pm 225$ nm from its center. The interparticle distance is denoted p.

particularly interesting antinodes within the (CDC) microcavity: one local maximum at the center of the active layer D (hence at the center of the photonic structure as a whole) and two larger maxima symmetrically located at the distance $\Delta = 225$ nm from that center. Note that the optical electric field amplitude at the center of the structure under consideration is slightly less than in the cladding layers C.

Increasing the impact of the 2D NP array requires it to coincide with an optical field antinode, where the intensity is large [7]. In the following, two such locations are considered and compared: at the center of the active layer D [Fig. 3(a)] and inside both layers C surrounding the active layer at distance $\Delta = \pm 225$ nm from that center [Fig. 3(b)]. In the latter case, two identical NP arrays are thus embedded in the microcavity.

All metallic NPs are assumed to have the same spheroidal shape and size and are characterized by aspect ratio $\xi = a_1/a_2$, where a_1 and a_2 are the half-lengths of their polar and equatorial axes, respectively. Furthermore, the NPs are also taken to form an ordered 2D array with a square unit cell whose translational invariance is directed along the x and y axes of the Cartesian coordinate system (see Fig. 3). In addition, all NPs are similarly aligned, with their polar axis parallel to the x axis. The typical dimensions of the NPs and the period p (interparticle distance) of the square lattice are supposed to be much smaller than the wavelength of the optical wave in the layers where the NP arrays are embedded, i.e., $\{2a_1, 2a_2, p\} \ll \lambda_0/\mathrm{Re}[\sqrt{\varepsilon_m}]$, $m = \{C, D\}$. Such a structure exhibits pronounced anisotropic optical properties, and its reflection and transmission spectra, in particular, are expected to depend significantly on the direction of polarization of the incident radiation [18,20].

3. TRANSFER MATRIX CALCULATIONS

The transfer matrix formalism is well adapted to the calculation of the optical properties of multilayered dielectric 1D heterostructures. It can be extended to the case of an embedded 2D metallic NP array as detailed below.

In the transfer matrix formalism, both interface matrices (accounting for reflection and refraction at any given interface) and propagation matrices (describing wave propagation within a given homogeneous layer) are needed. In the PC structures under study, the 2D NP arrays will be treated as interfaces.

In the first case [Fig. 3(a)], a total a of $(4N + 4)$ dielectric–dielectric interfaces and one 2D array of NPs must thus be taken into account, as well as $(4N + 4)$ dielectric layers (note that the central D layer is divided in two by the NP array).

In the second case [Fig. 3(b)], the number of dielectric–dielectric interfaces again amounts to $(4N + 4)$, the number of 2D NP arrays to two, and the number of dielectric layers to $(4N + 5)$.

In both cases, the first and the last interfaces separate a layer A from the vacuum. Hereinafter, the interfaces [including the 2D array(s) of NPs] internal to the heterostructure are numbered by the integer index j (with $2 \le j \le 4N + 3$ in the first case and $2 \le j \le 4N + 4$ in the second case), and the dielectric

layers they separate are numbered $(j-1)$ and j, following the positive direction of the z axis.

The well-known Fresnel formulas [36] give the expressions of the complex reflection (r_j^F) and refraction (t_j^F) coefficients at interface 'j'. Denoting ε_{j-1} and ε_j the respective relative dielectric permittivities of the non-magnetic dielectric layers it separates, and assuming that the electromagnetic wave impinges on the interface from layer '$j-1$' under normal incidence, these coefficients do not depend on the polarization of light; they read:

$$r_j^F = t_j^F - 1 = \frac{\sqrt{\varepsilon_{j-1}} - \sqrt{\varepsilon_j}}{\sqrt{\varepsilon_{j-1}} + \sqrt{\varepsilon_j}}. \tag{2a}$$

The Fresnel coefficients for the external boundaries of the structure are similarly given by

$$r_1^F = -r_{N'}^F = t_1^F - 1 = 1 - t_{N'}^F = \frac{1 - \sqrt{\varepsilon_A}}{1 + \sqrt{\varepsilon_A}}, \tag{2b}$$

where $N' = 4N + 5$ in the first case [Fig. 3(a)] and $N' = 4N + 6$ in the second case [Fig. 3(b)].

The reflection and refraction coefficients of the anisotropic metallic NP array surrounded on either side by an identical dielectric medium depends, even under normal incidence, on the state of polarization of the incoming wave. Denoting ε_p the relative permittivity of the metallic NPs and ε_m (equal to either the relative permittivity ε_C of GaAs or the effective-medium relative permittivity ε_D of the microcavity, depending on the location of the NP array) that of the isotropic dielectric layer into which the array is embedded, the complex reflection ($r_{x,y}^{\mathrm{NP}}$) and refraction ($t_{x,y}^{\mathrm{NP}}$) coefficients of a 2D NP array for two orthogonal linear polarizations (which will be called in the following the *longitudinal* and *transverse* states of polarization and correspond to the optical electric field oriented along the x and y axis, respectively) can be written, within the frame of the coupled-dipole approximation and for normal incidence, as [37,38]

$$r_{x,y}^{\mathrm{NP}} = t_{x,y}^{\mathrm{NP}} - 1 \approx i\frac{k_0\sqrt{\varepsilon_m}\alpha_{x,y}}{2p^2 - 0.72\alpha_{x,y}/p - ik_0\sqrt{\varepsilon_m}\alpha_{x,y}}, \tag{3}$$

where $k_0 = 2\pi/\lambda_0$ is the wavevector in free space and

$$\alpha_{x,y} = V\frac{\varepsilon_p - \varepsilon_m}{g_{x,y}(\varepsilon_p - \varepsilon_m) + \varepsilon_m} \tag{4}$$

is the complex polarizability of an individual spheroidal NP in an external optical field applied along the x or y axis [39]. In Eq. (4), $V = 4\pi a_1 a_2^2/3$ is the volume of the NP and $g_{x,y}$ is a geometric factor accounting for the influence of the shape of the NP on its induced dipolar moment. This factor is real and depends on the aspect ratio ξ with [39]

$$g_x = \frac{1}{1-\xi^2}\left(1 - \xi\frac{\arcsin\sqrt{1-\xi^2}}{\sqrt{1-\xi^2}}\right), \quad g_y = \frac{1}{2}(1 - g_x). \tag{5}$$

Equations (3)–(5) thus highlight the various parameters that control the response of the 2D NP array to the incoming electromagnetic wave, i.e., the dielectric properties of the NPs and the matrix in which they are embedded, the relative orientations of the anisotropy axes of the NPs and the polarization direction of the wave, and the structural parameters of the NP array itself (the shape and size of the NPs and the interparticle distance).

In a multilayered structure, waves resulting from successive reflections and refractions at the interfaces interfere, which results in overall complex optical electric fields E_f and E_b, where subscripts f and b refer to forward and backward waves with respect to the positive direction of the z axis, respectively. An interface matrix expresses the relationship between complex field amplitudes on either side of an interface. The matrix associated to the interface 'j' located at $z = z_j$ thus relates amplitudes $E_f(z_j^-)$ and $E_b(z_j^-)$ immediately before that interface to amplitudes $E_f(z_j^+)$ and $E_b(z_j^+)$ immediately after it with

$$\begin{pmatrix} E_f(z_j^-) \\ E_b(z_j^-) \end{pmatrix} = \hat{I}_j \begin{pmatrix} E_f(z_j^+) \\ E_b(z_j^+) \end{pmatrix}, \tag{6}$$

where the interface transfer matrix $\hat{I}_j$ takes a different form depending on which type of interface is considered. It is expressed as

$$\hat{I}_j^F = \frac{1}{t_j^F}\begin{pmatrix} 1 & r_j^F \\ r_j^F & 1 \end{pmatrix} \tag{7}$$

for a dielectric–dielectric interface and as

$$\hat{I}_{x,y}^{\mathrm{NP}} = \frac{1}{t_{x,y}^{\mathrm{NP}}}\begin{pmatrix} 1 & -r_{x,y}^{\mathrm{NP}} \\ r_{x,y}^{\mathrm{NP}} & 1 + 2r_{x,y}^{\mathrm{NP}} \end{pmatrix} \tag{8}$$

for a 2D NP array separating two identical dielectric layers [40] (for the sake of readability, index j is omitted in the latter case).

Similarly, the relationship between the complex field amplitudes at the boundaries of a homogeneous layer delimited by interfaces "$j-1$" and "j" can be written as

$$\begin{pmatrix} E_f(z_{j-1}^+) \\ E_b(z_{j-1}^+) \end{pmatrix} = \hat{P}_j \begin{pmatrix} E_f(z_j^-) \\ E_b(z_j^-) \end{pmatrix}, \tag{9}$$

where $\hat{P}_j$ is a propagation (or phase) matrix given by

$$\hat{P}_j = \begin{pmatrix} \exp(-i\delta_j) & 0 \\ 0 & \exp(i\delta_j) \end{pmatrix}, \tag{10}$$

and where $\delta_j = k_0\sqrt{\varepsilon_j}d_j$ is the phase thickness of the layer whose geometric thickness and relative dielectric permittivity are respectively d_j and ε_j.

Denoting L the total thickness of the system and applying Eqs. (6) and (9) to the entire PC, we obtain a relation between the amplitudes of the incident $E_i = E_f(0^-)$, reflected $E_r = E_b(0^-)$, and transmitted $E_t = E_f(L^+)$ optical fields as follows:

$$\begin{pmatrix} E_i \\ E_r \end{pmatrix} = \hat{G}_{x,y}\begin{pmatrix} E_t \\ 0 \end{pmatrix}, \tag{11}$$

where $\hat{G}_{x,y}$ is the overall transfer matrix of the structure and is obtained with

$$\hat{G}_{x,y} = \left(\prod_{j=1}^{2N+2}\hat{I}_j^{\mathrm{F}}\hat{P}_j\right)\hat{I}_{x,y}^{\mathrm{NP}}\left(\prod_{j=2N+3}^{4N+4}\hat{P}_j\hat{I}_{j+1}^{\mathrm{F}}\right) \tag{12}$$

for the structure shown in Fig. 3(a) and

$$\hat{G}_{x,y} = \left(\prod_{j=1}^{2N+1} \hat{I}_j^{\mathrm{F}} \hat{P}_j\right) \hat{I}_{x,y}^{\mathrm{NP}} \left(\prod_{j=2N+2}^{2N+3} \hat{P}_j \hat{I}_{j+1}^{\mathrm{F}}\right) \hat{P}_{2N+4}\ \hat{I}_{x,y}^{\mathrm{NP}} \times \left(\prod_{j=2N+5}^{4N+5} \hat{P}_j \hat{I}_{j+1}^{\mathrm{F}}\right) \tag{13}$$

for the structure depicted in Fig. 3(b). Note that Eq. (13) is written for the case of identical 2D arrays. Propagation matrices $\hat{P}_{2N+2}$ and $\hat{P}_{2N+3}$ in Eq. (12) are obtained for a geometric thickness equal to $d_D/2$. Similarly, propagation matrices $\hat{P}_{2N+1}$, $\hat{P}_{2N+2}$, $\hat{P}_{2N+4}$, and $\hat{P}_{2N+5}$ in Eq. (13) correspond to layers whose geometric thicknesses are equal to $(d_D/2 + d_C - \Delta)$, $(\Delta - d_D/2)$, $(\Delta - d_D/2)$, and $(d_D/2 + d_C - \Delta)$, respectively.

The reflectivities $R_{x,y}$ and transmittivities $T_{x,y}$ of the entire photonic structure for the longitudinal and transverse light polarizations can then be calculated as

$$R_{x,y} = \left|\frac{E_r}{E_i}\right|^2 = \left|\frac{(\hat{G}_{x,y})_{21}}{(\hat{G}_{x,y})_{11}}\right|^2, \quad T_{x,y} = \left|\frac{E_t}{E_i}\right|^2 = \frac{1}{|(\hat{G}_{x,y})_{11}|^2}. \tag{14}$$

4. RESULTS AND DISCUSSION

Let us first consider the active structure without an embedded 2D NP array (Fig. 1). As expected (see Section 2), its transmission spectrum (Fig. 4) exhibits a photonic bandgap centered on $\lambda_0 = 1.55$ μm and a defect mode situated at that precise wavelength. Due to the presence of the active composite microcavity, the transmittivity associated to that defect mode greatly exceeds 1 (see the inset in Fig. 4). This structure does not include any anisotropic elements, so the efficiency of the amplification of the defect mode does not depend on the state of polarization of the incoming electromagnetic wave.

Let us then illustrate qualitatively the transmission properties of the NP array itself. In order to assess its sole contribution, calculations are carried out with two semi-infinite GaAs layers surrounding the metallic NP array.

The NPs have the shape of prolate (i.e., elongated) spheroids (and thus with $a_1 > a_2$, i.e., $\xi > 1$) with a half-length of the polar axis $a_1 = 10$ nm, and they are made of silver (Ag). The typical particle density of NPs is thus of the order of 100 particles per square micrometer (μm^2) in the array. Their relative permittivity is taken to follow the Drude model with

$$\varepsilon_p(\omega) = \varepsilon_\infty - \frac{\omega_p^2}{\omega^2 + i\omega\gamma}, \tag{15}$$

where $\omega_p = 1.35 \times 10^{16}$ rad.s^{-1} is the plasma frequency in silver, $\varepsilon_\infty = 5$ is the contribution of its crystal lattice, and $\gamma = 5.5 \times 10^{13}$ s^{-1} is the relaxation rate describing the effective electron scattering rate in that crystal [41]. The calculations are carried out taking into account the frequency dispersion of the dielectric permittivity of GaAs [34].

Figures 5 and 6 show the transmittivity $|t_{x,y}^{\mathrm{NP}}|^2$ of the 2D NP array for the longitudinal polarization (optical electric field directed along the polar axis of the metallic spheroids) and the transverse polarization (optical electric field directed perpendicular to that axis) of the incoming light. Dips in transmittivity spectra correspond to light wavelengths coinciding with the excitation of surface plasmon resonances in the spheroidal silver particles. Due to the anisotropy of the particles [see shape factors g_x and g_y in

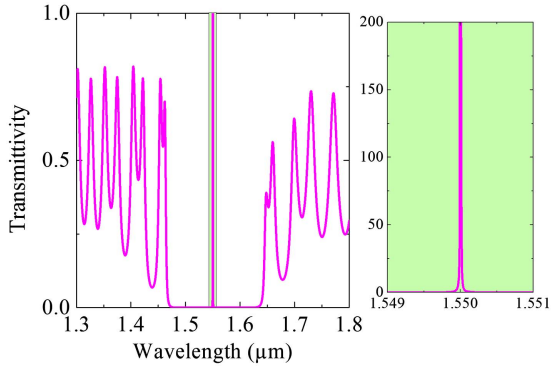

Fig. 4. Transmission spectrum of the photonic structure without a NP array. The spectrum is identical for any direction of the plane of polarization of the incident light wave. The inset zooms the spectrum around the defect mode (note the different vertical scale in the inset and in the main figure).

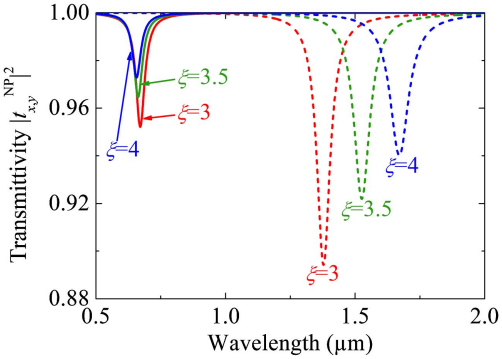

Fig. 5. Transmission spectra of an Ag NP array embedded in a GaAs matrix for the longitudinal (dashed lines) and transverse (solid lines) polarization states of the incoming light wave and for values of the aspect ratio ξ of the NPs equal to 3 (red lines), 3.5 (green lines), and 4 (blue lines). The period of the NP array is $p = 120$ nm. The length of the polar axis of the NPs is $2a_1 = 20$ nm.

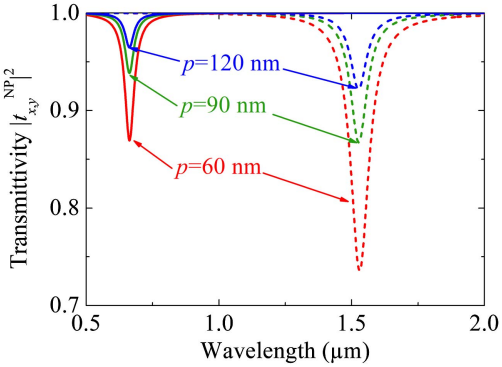

Fig. 6. Transmission spectra of an Ag NP array embedded in a GaAs matrix for the longitudinal (dashed lines) and transverse (solid lines) polarization states of the incoming light wave and for values of the period p of the NP array equal to 60 nm (red lines), 90 nm (green lines), and 120 nm (blue lines). The aspect ratio of the NPs is $\xi = 3.5$. The length of the polar axis of the NPs is $2a_1 = 20$ nm.

Eq. (5)], these resonances do not occur at the same wavelength for longitudinal and transverse polarization states.

In Fig. 5, the effect of the aspect ratio ξ of the NPs on these resonances is highlighted. The latter occur at larger wavelengths for the longitudinal incoming state of polarization (in the near-infrared domain) than for the transverse polarization state (in the visible domain).

For each of the three values of ξ considered ($\xi = 3$, 3.5, and 4) the amplitude of the plasmon resonance is also approximately twice larger for longitudinally polarized light, for which the dipolar moment induced in each NP is larger than for transversally polarized light. This can mostly be associated with the fact that in the latter case the resonance takes place in a spectral domain for which optical absorption in the GaAs layers surrounding the NP array is larger than around 1.55 μm.

Furthermore, for both incoming states of polarization, increasing the value of the aspect ratio ξ reduces the amplitude of the surface plasmon resonance. This can be related to the fact that for a given value of the half-length a_1 of the polar axis, the volume of the prolate spheroidal NPs decreases when ξ increases, which in turn reduces the overall efficiency of surface plasmon excitation.

Moreover, reducing the value of aspect ratio ξ brings the surface plasmon resonances for transverse and longitudinal incoming states of polarization closer to each other (hence, there is a red-shift for the former and a blue-shift for the latter), as the spheroids thus tend towards a spherical shape, for which transverse and longitudinal resonances are expected to merge.

Figure 6 illustrates the influence of the period p of the 2D NP array on its transmittivity spectrum for a given value of aspect ratio $\xi = 3.5$. Again, comparisons are made between three cases, namely, for $p = 60$, 90, and 120 nm. Here, of course, increasing the value of p has very little effect on the spectral position of the surface plasmon resonances, as it does not affect the shape of the NPs. It does, however, reduce the amplitude of the transmission dips due to surface plasmon resonance, which is in agreement with the decreasing surface density of silver NPs in the 2D layer when the interparticle distance increases—hence the decreasing impact of surface plasmon excitation on light scattering.

Figures 5 and 6 show how the spectral characteristics of the 2D array of NPs significantly depend on both the shape of the NPs and the surface density of the NPs in the array. On the basis of simulation results such as those presented in these figures, we can determine the structural parameters of the 2D NP array that will enhance the sensitivity of the spectral behavior of the entire PC structure to the polarization of the incoming light beam. In the following, we focus on the case where the surface plasmon resonance of the NP array coincides with the defect mode centered on wavelength $\lambda_0 = 1.55$ μm.

It should be noted, however, that the spectral characteristics of the NP array are bound to vary with the location of the array within the structure—in the active layer D or in the GaAs cladding layers C of the microresonator—due to differences in their dielectric permittivities (as mentioned above, the spectra shown in Figs. 5 and 6 have been obtained for a semi-infinite GaAs layer on either side of the array). In the following, we consider values of the aspect ratio ξ that ensure that the collective *longitudinal* surface plasmon resonance of the 2D silver NPs array(s) coincides with $\lambda_0 = 1.55$ μm for both situations described in Section 2. Specifically, using Eqs. (3)–(5), we determined that this condition is achieved for $\xi = 3.6$ when two NP arrays are symmetrically embedded in the cladding layers C and for $\xi = 3.2$ when a single NP array is located at the center of the active region D.

Furthermore, according to Eq. (4), the polarizability and hence the spectral characteristics of the NPs also depends on their volume, which, for a given value of aspect ratio ξ, is proportional to the third power of the half-length a_1 of their polar axis. This opens up additional possibilities of controlling the spectral response of the 2D NP array. In particular, an increase in the polar axis length of the NPs leads to an increase in the scattering efficiency and absorption of a light wave by the 2D NP array. In order to simplify the analysis in this paper, we have restricted ourselves to the case of NPs with a fixed dimension of their polar axis.

Calculated transmission spectra $T_x(\lambda_0)$ of the photonic structure including one ($\xi = 3.6$) or two ($\xi = 3.2$) NP arrays are shown in Fig. 7(a) for a longitudinal polarization of the incoming light. As in Fig. 6, three values of the interparticle distance p are considered. The main figure (solid purple line) shows a spectrum, away from the spectral domain immediately surrounding $\lambda_0 = 1.55$ μm, that does not depend much on the value of p. It clearly appears that this part of the spectrum closely follows that of the photonic structure without a NP array shown in Fig. 4. The effect of the value of p, on the other

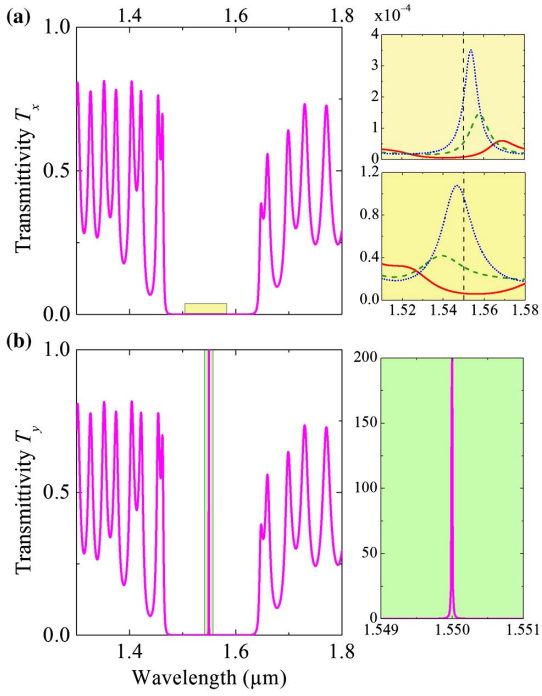

Fig. 7. (a) Transmission spectra T_x (λ_0) of the amplifying PC with one (top inset) and two (bottom inset) embedded silver 2D NP array(s) for an interparticle distance p equal to 60, 90, and 120 nm (red, green, and blue lines, respectively, in the insets). The dashed vertical line in the insets denotes the wavelength $\lambda_0 = 1.55$ μm. (b) Transmission spectrum T_y (λ_0) for both geometries of the PC shown in Fig. 3 and for 60 nm $\leq p \leq$ 120 nm. The insets zoom in on the spectral region surrounding the defect mode.

hand, manifests itself for wavelengths close to that of the defect mode in the structure without a NP array, where the spectra for $p = 60$ nm (solid red line), 90 nm (dashed green line), and 120 nm (dotted blue line) are shown in the insets of Fig. 7(a) for a single NP array located at the center of the PC (top inset) and for two NP arrays located at an equal distance Δ from that center (bottom inset), respectively. Comparing Figs. 4 and 7(a) thus shows that the excitation of the longitudinal surface plasmon resonance in silver NPs results in a drastic decay (almost a complete suppression) of the defect mode of the x-polarized component of the transmittivity. This can in part be attributed to large ohmic losses of the electromagnetic wave in resonant interaction with the metallic NPs. A second reason for the quasi-suppression of the defect mode in $T_x(\lambda_0)$ can be found in the modification of the spectrum of the PC structure (the shift of its defect mode) due to the complex influence of the resonant NP array(s) on the phases of the electromagnetic waves that interfere in the multilayered PC. Consequently, this spectral shift depends on the position of the NP array(s) in the heterostructure: as can be seen in the insets of Fig. 7(a), for a single NP array placed at the center of the PC, the defect mode experiences a red-shift when the interparticle distance p decreases (top inset), whereas for two NP arrays symmetrically located in the lateral layers C of the microcavity, a blue-shift of the defect mode is observed (bottom inset). In both cases, for smaller values of p (typically, below 90 nm) the peak of the defect mode shifts toward one of the bandgap edges so that the longitudinal transmittivity T_x at wavelength $\lambda_0 = 1.55$ μm becomes close to zero [see, for instance, the solid red lines in the insets of Fig. 7(a) for $p = 60$ nm].

Comparing the insets in Fig. 7(a), one can see that the amplitude of what remains of the defect mode when it is nearly suppressed by two NP arrays placed in layers C is about three times smaller than its amplitude when a single NP array at the center of the PC provokes its quasi-extinction. This can be related to the larger number of scattering centers (surface plasmons excited in the NPs) in the former case. However, even in the latter case, the intensity of the transmitted wave is almost negligible, as in both cases the reduction rate of the intensity is of the order of 10^6 with respect to the structure without a NP array. Moreover, additional calculations show that a similar suppression of the defect mode in the longitudinal transmission spectrum $[T_x(\lambda_0)]$ of the heterostructure can be achieved even with a single NP array placed at a distance $\Delta = 225$ nm on either side of the center of the structure. In short, the presence of a single NP array at a location where it can interact resonantly with a maximum of the optical field is enough to inhibit the defect mode in the transmission spectrum of an incoming x-polarized light wave.

Figure 7(b) shows that the influence of the NP array(s) on the transmission spectrum $T_y(\lambda_0)$ of an incoming transverse polarized light wave is entirely different. This spectrum appears virtually identical to that of the PC structure without 2D array(s) of silver NPs (see Fig. 4), and the amplification of the defect mode (by a factor of at least 200) due to the active microcavity at the center of the structure remains unchanged, whatever the location or the period (or, as further calculations easily demonstrate, the aspect ratio) of the NP array(s). This is evidently due to the fact that in this case the wavelength of the incoming light wave is much too distant from the wavelengths of the plasmon resonances (see the solid lines in Figs. 5 and 6) to be able to excite them, so the presence of the NP array does not significantly affect the amplification of the defect mode for a y-polarized light wave.

As a result, our calculations demonstrate the feasibility of using an active multilayered photonic crystal with intracavity 2D arrays of metallic NPs in order to allow the transmission of an amplified defect mode, or on the contrary to prevent it, depending on the choice of the polarization of the linearly polarized incoming light beam. For any polarization state of that beam, the heterostructure thus acts as a narrow-band amplifying polarizer.

5. CONCLUSIONS

In this paper, we have demonstrated that polarization-controlled amplification of a defect mode can be achieved in an amplifying photonic crystal in which periodic 2D arrays of metallic nanoparticles are embedded. In our calculations, the thicknesses of the layers constituting a VCSEL-type cavity surrounded by two identical dielectric DBRs were chosen so that the structure exhibits a defect mode at a vacuum wavelength 1.55 μm. In the absence of a 2D nanoparticle array, this defect mode is amplified by the active cavity placed at the center of the system. The presence of one or several 2D nanoparticle arrays embedded in the multilayered heterostructure provides a polarization-dependent way to suppress the defect mode. This can be achieved if the dimensions and mutual distance of the spheroidal nanoparticles are chosen so that a surface plasmon resonance is excited in them by an incoming light beam of 1.55 μm vacuum wavelength coinciding with the defect mode.

Specifically for that wavelength, the component of the optical field parallel to the long axis of the spheroidal particles is in resonant interaction with a surface plasmon and is thus efficiently suppressed, whereas the component of the field parallel to their short axis does not interact much with them but gets amplified by the active cavity. As a result, the system acts as a narrow-band amplifying polarizer. We show that the suppression of the defect mode in the former case is most efficient when the nanoparticle array is embedded at locations of maximal optical field localization in the amplifying region of the structure.

Moreover, the approach discussed in this paper, in combination with other recently proposed solutions (based, for instance, on the use of liquid crystals [42–44] or of materials whose properties can be magnetically or electrically controlled [45–49]), can significantly expand the possibilities of controlling the polarization of light emitted by semiconductor lasers.

In addition, it is interesting to note that this configuration could provide a promising way to control the polarization of resonant modes for significantly lower intensities of the emitted radiation if the cavity included nonlinear (e.g., Kerr-type) media.

Funding. Russian Foundation for Basic Research (RFBR) (18-42-730007); Conseil Régional de Bretagne, France (PhotoMag, SPEACS); Ministry of Education and Science of the Russian Federation (Minobrnauka) (075-00629-19-00, 3.5698.2017/9.10, 3.7614.2017/9.10); École Nationale d'Ingénieurs de Brest, France (HF-CCCP).

REFERENCES

1. L. Novotny and N. van Hulst, "Antennas for light," Nat. Photonics **5**, 83–90 (2011).
2. F. Ding, A. Pors, and S. I. Bozhevolnyi, "Gradient metasurfaces: a review of fundamentals and applications," Rep. Prog. Phys. **81**, 026401 (2018).
3. R. Kullock, S. Grafström, P. R. Evans, R. J. Pollard, and L. M. Eng, "Metallic nanorod arrays: negative refraction and optical properties explained by retarded dipolar interactions," J. Opt. Soc. Am. B **27**, 1819–1827 (2010).
4. S. G. Moiseev, "Active Maxwell-Garnett composite with the unit refractive index," Physica B **405**, 3042–3045 (2010).
5. A. I. Rahachou and I. V. Zozoulenko, "Light propagation in nanorod arrays," J. Opt. A **9**, 265–270 (2007).
6. S. G. Moiseev and V. A. Ostatochnikov, "Defect modes of one-dimensional photonic-crystal structure with a resonance nanocomposite layer," Quantum Electron. **46**, 743–748 (2016).
7. S. G. Moiseev, I. A. Glukhov, V. A. Ostatochnikov, A. P. Anzulevich, and S. N. Anzulevich, "Spectra from a photonic crystal structure with a metallic nanoparticle monolayer," J. Appl. Spectrosc. **85**, 511–516 (2018).
8. S. Y. Vetrov, R. G. Bikbaev, and I. V. Timofeev, "The optical Tamm states at the edges of a photonic crystal bounded by one or two layers of a strongly anisotropic nanocomposite," Opt. Commun. **395**, 275–281 (2016).
9. H. A. Elsayed, "Transmittance properties of one dimensional ternary nanocomposite photonic crystals," Mater. Res. Express **5**, 036209 (2018).
10. A. H. Aly, C. Malek, and H. A. Elsayed, "Transmittance properties of a quasi-periodic one-dimensional photonic crystals that incorporate nanocomposite material," Int. J. Mod. Phys. B **32**, 1850220 (2018).
11. V. S. Gerasimov, A. E. Ershov, R. G. Bikbaev, I. L. Rasskazov, I. V. Timofeev, S. P. Polyutov, and S. V. Karpov, "Engineering mode hybridization in regular arrays of plasmonic nanoparticles embedded in 1D photonic crystal," J. Quant. Spectrosc. Radiat. Transf. **224**, 303–308 (2019).
12. P. Alivisatos, "The use of nanocrystals in biological detection," Nat. Biotechnol. **22**, 47–52 (2004).
13. S. Unser, I. Bruzas, J. He, and L. Sagle, "Localized surface plasmon resonance biosensing: current challenges and approaches," Sensors **15**, 15684–15716 (2015).
14. S. G. Moiseev, "Composite medium with silver nanoparticles as an anti-reflection optical coating," Appl. Phys. A **103**, 619–622 (2011).
15. A. S. Shalin and S. G. Moiseev, "Controlling interface reflectance by a monolayer of nanoparticles," Quantum Electron. **39**, 1175–1181 (2009).
16. X. Tang, L. Zhou, X. Du, and Y. Yang, "Enhancing absorption properties of composite nanosphere and nanowire arrays by localized surface plasmon resonance shift," Results Phys. **7**, 87–94 (2017).
17. T. P. Otanicar, P. E. Phelan, R. S. Prasher, G. Rosengarten, and R. A. Taylor, "Nanofluid-based direct absorption solar collector," J. Renew. Sust. Energy **2**, 033102 (2010).
18. S. G. Moiseev, "Nanocomposite-based ultrathin polarization beam-splitter," Opt. Spectrosc. **111**, 233–240 (2011).
19. Ö. Sepsi, T. Gál, and P. Koppa, "Polarized light emitting diodes using silver nanoellipsoids," Opt. Express **22**, A1190–A1196 (2014).
20. V. Lozovski and M. Razumova, "Influence of inclusion shape on light absorption in thin Au/Teflon nanocomposite films," J. Opt. Soc. Am. B **33**, 8–16 (2016).
21. S. G. Moiseev, V. A. Ostatochnikov, and D. I. Sementsov, "Defect mode suppression in a photonic crystal structure with a resonance nanocomposite layer," Quantum Electron. **42**, 557–560 (2012).
22. S. Y. Vetrov, P. S. Pankin, and I. V. Timofeev, "Peculiarities of spectral properties of a one-dimensional photonic crystal with an anisotropic defect layer of the nanocomposite with resonant dispersion," Quantum Electron. **44**, 881–884 (2014).
23. R. Michalzik, ed., *VCSELs. Fundamentals, Technology and Applications of Vertical-Cavity Surface-Emitting Lasers* (Springer-Verlag, 2013).
24. D.-S. Song, S.-H. Kim, H.-G. Park, C.-K. Kim, and Y.-H. Lee, "Single-fundamental-mode photonic-crystal vertical-cavity surface-emitting lasers," Appl. Phys. Lett. **80**, 3901–3903 (2002).
25. M. A. Arteaga, M. López-Amo, H. Thienpont, and K. Panajotov, "Role of external cavity reflectivity for achieving polarization control and stabilization of vertical cavity surface emitting laser," Appl. Phys. Lett. **90**, 031117 (2007).
26. Y. Hong, R. Ju, P. S. Spencer, and K. A. Shore, "Investigation of polarization bistability in vertical-cavity surface-emitting lasers subjected to optical feedback," IEEE J. Quantum Electron. **41**, 619–624 (2005).
27. J. M. Ostermann, P. Debernardi, and R. Michalzik, "Optimized integrated surface grating design for polarization-stable VCSELs," IEEE J. Quantum Electron. **42**, 690–698 (2006).
28. J. Hashizume and F. Koyama, "Transverse and polarization mode controlled vertical cavity surface emitting laser with metal nano-aperture array for optical near-field," in *18th Annual Meeting of the IEEE Lasers and Electro-Optics Society, LEOS*, Oct. 2005, paper WK3, pp. 467–468.
29. P. Babu Dayal and F. Koyama, "Polarization control of 0.85 μm vertical-cavity surface-emitting lasers integrated with gold nanorod arrays," Appl. Phys. Lett. **91**, 111107 (2007).
30. J. D. Joannopoulos, R. D. Meade, and J. N. Winn, *Photonic Crystals* (Princeton University, 1995).
31. K. Inoue and K. Ohtaka, eds., *Photonic Crystals: Physics, Fabrication and Applications* (Springer-Verlag, 2004).
32. Y. Dadoenkova, I. Glukhov, S. Moiseev, V. Svetukhin, A. Zhukov, and I. Zolotovskii, "Optical generation in an amplifying photonic crystal with an embedded nanocomposite polarizer," Opt. Commun. **389**, 1–4 (2017).
33. M. A. Rahman, M. R. Karim, J. Akhtar, and M. I. Reja, "Performance characterization of a GaAs based 1550 nm $Ga_{0.591}In_{0.409}N_{0.028}As_{0.89}Sb_{0.08}$ MQW VCSEL," Int. J. Photon. Opt. Technol. **4**, 14–18 (2018).
34. A. D. Rakić and M. L. Majewski, "Modeling the optical dielectric function of GaAs and AlAs: extension of Adachi's model," J. Appl. Phys. **80**, 5909–5914 (1996).
35. A. Sihvola, *Electromagnetic Mixing Formulas and Applications* (Institution of Electrical Engineers, 1999).
36. M. Born and E. Wolf, *Principles of Optics* (Cambridge University, 1999).
37. E. F. Kuester, M. A. Mohamed, M. Piket-May, and C. L. Holloway, "Averaged transition conditions for electromagnetic fields at a metafilm," IEEE Trans. Antennas Propag. **51**, 2641–2651 (2003).
38. C. L. Holloway, M. A. Mohamed, E. F. Kuester, and A. Dienstfrey, "Reflection and transmission properties of a metafilm: with an application to a controllable surface composed of resonant particles," IEEE Trans. Electromagn. Compat. **47**, 853–865 (2005).
39. C. F. Bohren and D. R. Huffman, *Absorption and Scattering of Light by Small Particles* (Wiley, 1983).
40. C. C. Katsidis and D. I. Siapkas, "General transfer-matrix method for optical multilayer systems with coherent, partially coherent, and incoherent interference," Appl. Opt. **41**, 3978–3987 (2002).
41. H. U. Yang, J. D'Archangel, M. L. Sundheimer, E. Tucker, G. D. Boreman, and M. B. Raschke, "Optical dielectric function of silver," Phys. Rev. B **91**, 235137 (2015).
42. L. Frasunkiewicz, T. Czyszanowski, H. Thienpont, and K. Panajotov, "Electrically tunable VCSEL with intra-cavity liquid crystal: design, optimization, and analysis of polarization- and mode-stability," Opt. Commun. **427**, 271–277 (2018).
43. H. Mehrzad and E. Mohajerani, "Liquid crystal mediated active nanoplasmonic based on the formation of hybrid plasmonic-photonic modes," Appl. Phys. Lett. **112**, 061101 (2018).
44. V. A. Gunyakov, I. V. Timofeev, M. N. Krakhalev, W. Lee, and V. Y. Zyryanov, "Electric field-controlled transformation of the eigenmodes in a twisted-nematic Fabry-Pérot cavity," Sci. Rep. **8**, 16869 (2018).
45. C.-J. Wu, J.-J. Liao, and T.-W. Chang, "Tunable multilayer Fabry-Perot resonator using electro-optical defect layer," J. Electromagn. Waves Appl. **24**, 531–542 (2010).
46. L. He, Y. Hu, H. Kim, J. Ge, S. Kwon, and Y. Yin, "Magnetic assembly of nonmagnetic particles into photonic crystal structures," Nano Lett. **10**, 4708–4714 (2010).
47. T. Goto, H. Sato, H. Takagi, A. V. Baryshev, and M. Inoue, "Novel magnetophotonic crystals controlled by the electro-optic effect for nonreciprocal high-speed modulators," J. Appl. Phys. **109**, 07B756 (2011).
48. V. G. Arkhipkin, V. A. Gunyakov, S. A. Myslivets, V. Y. Zyryanov, V. F. Shabanov, and W. Lee, "Electro- and magneto-optical switching of defect modes in one- dimensional photonic crystals," J. Exp. Theor. Phys. **112**, 577–587 (2011).
49. A. H. Aly, H. A. Elsayed, A. A. Ameen, and S. H. Mohamed, "Tunable properties of one-dimensional photonic crystals that incorporate a defect layer of a magnetized plasma," Int. J. Mod. Phys. B **31**, 1750239 (2017).